ACCSCIENCE PUBLISHING

International Journal of Bioprinting

SHORT COMMUNICATION

Microfluidic bioprinting of cell-laden gradients in RADA16-I self-assembling peptide hydrogels

Maximilian Jergitsch[1,2], Soledad Perez-Amodio[1,2], Luis M. Delgado[1,2], Roman A. Perez[1,2], and Miguel A. Mateos-Timoneda[1,2]*

[1]Bioengineering Institute of Technology, Universitat Internacional de Catalunya, Barcelona, Spain

[2]Department of Bioengineering, Faculty of Medicine and Health Science, Universitat Internacional de Catalunya, Barcelona, Spain

Abstract

Reproducing the continuous compositional and cellular transitions found in native tissues remains a major challenge in extrusion-based bioprinting, which typically generates constructs composed of discrete regions and imposes stringent rheological requirements on bioinks. Microfluidic bioprinting offers new opportunities to reproduce tissue heterogeneity by enabling controlled mixing of biomaterials and cell populations during extrusion. In this study, we present a coaxial microfluidic bioprinting strategy for fabricating hydrogel scaffolds with continuous cellular gradients using low-viscosity self-assembling peptide bioinks. The system combines three independently controlled syringe pumps with a 3D-printed coaxial nozzle containing a screw-like passive mixer. Two low-viscosity RADA16-I peptide solutions containing different cell populations are mixed in situ, while a methylcellulose–alginate shell stabilizes the filament during printing and supports post-printing self-assembly of the core hydrogel. Computational simulations confirm efficient mixing within the nozzle, and fluorescence imaging demonstrates smooth compositional transitions along printed filaments. The system enables the fabrication of scaffolds containing co-culture gradients of endothelial cells and mesenchymal stem cells, which remain viable and display cell-type-specific organization. Overall, this approach enables the printing of soft peptide hydrogels and the fabrication of biomimetic constructs with continuous cellular transitions, highlighting its potential for tissue engineering and regenerative medicine.

Keywords: Tissue engineering; Coaxial 3D extrusion bioprinting; Cell gradients; Static mixer; Self-assembling peptide hydrogel

***Corresponding author:**
Miguel A. Mateos-Timoneda
(mamateos@uic.es)

Citation: Jergitsch M, Perez-Amodio S, Delgado LM, Perez RA, Mateos-Timoneda MA. Microfluidic bioprinting of cell-laden gradients in RADA16-I self-assembling peptide hydrogels. *Int J Bioprint*. 2026;12(3):026120104.
doi: 10.36922/IJB026120104

Received: March 20, 2026

Revised: April 27, 2026

Accepted: April 29, 2026

Published online: May 1, 2026

1. Introduction

Tissue engineering and regenerative medicine seek to restore or replace damaged tissues by recreating the spatial and temporal organization of cells and extracellular matrix (ECM).[1] Native tissues exhibit hierarchical organization, in which distinct yet interdependent cellular and ECM layers collectively define tissue function.[2-5] Importantly, these structural features are often connected through gradual transitions in cell phenotype, ECM composition, and mechanical properties rather than abrupt interfaces.[6,7] Three-dimensional (3D) bioprinting has emerged as a promising

technology that enables the controlled deposition of cells and biomaterials to reproduce such spatial complexity.[8-10] Among available approaches, extrusion-based bioprinting remains widely used due to its cost-effectiveness, material versatility, and compatibility with multimaterial and multicellular constructs.[11]

Despite its great potential for tissue engineering and regenerative medicine, extrusion-based bioprinting still faces important limitations. Compositional heterogeneity is typically achieved by switching between separate printheads dispensing distinct bioink formulations, resulting in constructs composed of discrete regions rather than continuous transitions.[12-14] In addition, extrusion printing imposes strict rheological requirements on bioinks to ensure filament formation and structural stability.[15,16] Many biologically favorable hydrogels, therefore, require modification or additional processing strategies to achieve sufficient printability while maintaining structural integrity post-printing.

To overcome these challenges, microfluidic bioprinting leverages fluid manipulation within microscale channels to enable precise control over bioink flow, mixing, and composition during extrusion.[17,18] By combining multiple ink streams within a single printhead, this approach allows continuous modulation of material composition during deposition. Such control enables the fabrication of seamless gradients in cell density, biomaterial composition, or bioactive factors within individual filaments, while facilitating the processing of low-viscosity bioinks through in situ stabilization or gelation strategies.[19,20]

One such strategy is the coextrusion of a load-bearing shell material, which effectively reduces the mechanical and rheological constraints on the core bioink.[21,22] The shell stabilizes the liquid core during extrusion, enabling the printing of soft or slow-gelling biomaterials that would otherwise lack sufficient structural integrity. For example, coextrusion with a highly viscous methylcellulose (MC)-based shell has enabled the printing of extremely soft RADA16-I peptide hydrogels while maintaining structural fidelity and supporting nutrient diffusion during culture.[23]

Building on this concept, the present study advances coaxial bioprinting by enabling simultaneous operation of three extruders. The primary extruder delivered the shell material into a coaxial nozzle, while two additional extruders supplied RADA16-I core solutions containing distinct cell populations: human umbilical vein endothelial cells (HUVECs) and mesenchymal stem cells (MSCs). An integrated screw-like mixer within the coaxial nozzle enabled in situ mixing of the two cell suspensions prior to extrusion. This configuration enabled the fabrication of hydrogel scaffolds with continuous gradients between the two cell populations, thereby overcoming the limitations of discrete material transitions in the fabrication of biomimetic tissue constructs.

2. Materials and methods

2.1. Materials

Methylcellulose (4,000 cP), phosphate-buffered saline (PBS) tablets, sucrose, HEPES, calcium chloride, α-minimum essential medium (αMEM), research-grade fetal bovine serum (FBS), penicillin–streptomycin cocktail (P/S), trypsin-ethylenediaminetetraacetic acid (EDTA), paraformaldehyde, Triton X-100, phalloidin-Atto 488, and DAPI ready-made solution were all purchased from Sigma-Aldrich (United States of America [USA]). Sodium hydroxide was acquired from Merck KGaA (Germany). Bone marrow-derived MSCs, Vascular Cell Basal Medium, and Endothelial Cell Growth Kit-VEGF were purchased from ATCC (USA). HUVECs were purchased from PromoCell (Germany). DPBS solution, propidium iodide (PI), calcein AM, GlutaMAX™, CellTracker™ Deep Red, CellTracker™ Green CMFDA, and sterile syringe filters (polyethersulfone, 0.2 μm, 25 mm) were purchased from Thermo Fisher Scientific (USA). Sodium alginate was purchased from AppliChem (350–550 mPa·s for 1% solution at 20°C; Germany). RADA16-I peptide with >95% purity was purchased from Abyntek Biopharma (Spain). Liqcreate Clear Impact transparent resin was purchased from 3DJake (Austria). Isopropyl alcohol 99.9% was purchased from 3D-basics (Austria).

2.2. Preparation of shell and core hydrogel

2.2.1. Methylcellulose–alginate shell hydrogel

The shell bioink was prepared by dissolving 1% (w/v) sodium alginate powder in a solution containing 3× PBS and 10% (w/v) sucrose. The prepared sodium alginate solution and MC powder were steam-sterilized at 121 °C for 15 min. Under aseptic conditions, 7% (w/v) MC was dissolved in preheated sodium alginate solution (70 °C) using a SpeedMixer DAC 150.1 FVZ (FlackTek, USA) at 50 × g for 5 min. The shell bioink formulation was stored at 4 °C overnight for complete hydration.

2.2.2. RADA16-I core hydrogel

The core bioink was prepared by dissolving RADA16-I peptide powder in Milli-Q water. Separately, steam-sterilized MC powder was dissolved in a filter-sterilized, preheated solution at 70 °C containing 30% (w/v) sucrose. Under aseptic conditions, the solution was mixed using the SpeedMixer at 700 rpm for 5 min and stored at 4 °C overnight. In the final step, 0.5% (w/v) MC solution was mixed with 1% (w/v) RADA16-I peptide solution at a

volume ratio of 0.85:0.15 (MC:RADA16-I), yielding final concentrations of 0.425% MC and 0.15% RADA16-I. This formulation is referred to as RADA-MC.

2.3. Fabrication of coaxial nozzle

The nozzle (inner diameter: 320 μm, outer diameter: 1 mm) was printed using a Phrozen Sonic Mighty 8K (Phrozen Tech, Taiwan) with Liqcreate Clear Impact photopolymer resin (Liqcreate, The Netherlands). Layer height was set to 25 μm. The nozzles were oriented so that their upper surfaces contacted the build platform, thereby avoiding the need for support structures. After printing, the nozzles were rinsed in isopropanol, then dried using compressed air. The nozzles were post-cured under UV light for 1 h in the Elegoo Mercury Plus UV chamber (Elegoo, China) and left at 60 °C overnight.

2.4. Computational fluid dynamics analysis of mixing performance

Finite element fluid flow simulations were performed in COMSOL Multiphysics 6.0 software (COMSOL AB, USA), and 3D models were imported using the LiveLink™ for SOLIDWORKS® (SolidWorks 2024, Dassault Systèmes, France) add-on. A stationary laminar-flow simulation was performed using a physics-controlled mesh set to normal size. The mass flow rates used in the computational fluid dynamics simulation were based on empirical findings from printing at 3 mm/s. The total mass flow rate through the two core inlets was set to 2 mg/s. A parametric sweep was performed to evaluate mixing performance at different inlet-mass-flow ratios for the two core inlets (1:3, 1:1, and 3:1). Bioink properties were modeled as an inelastic, non-Newtonian fluid (flow behavior index = 1.53, consistency coefficient = 0.257).[23]

2.5. Core–shell 3D printing

A custom-modified printer and coaxial nozzle were used for core–shell printing, as described previously.[21] Integrating the Bigtreetech BTT EXP-MOT V1.0 into the previously presented 3D extrusion bioprinter setup enabled simultaneous control of three syringe extruders. The coaxial nozzle was mounted to the primary syringe extruder, which directly fed the shell bioink. The second and third syringe extruders delivered the core bioinks through flexible silicone tubing (inner diameter = 0.6 mm) connected to the coaxial nozzle. Printing parameters were set to 4 mm/s and 2.9 μL/s for printing speed and extrusion rate, respectively. The print bed temperature was set to 37 °C for all experiments.

2.6. Rhodamine B staining of core hydrogel

Rhodamine B staining solution was added to the RADA16-I core solution to a final concentration of 10 μM. The printed hydrogel scaffolds were imaged using a Leica TCS SP8 (Germany) confocal laser scanning microscope (CLSM) with excitation and emission wavelengths set to 550 nm and 630 nm, respectively. To assess the distribution of Rhodamine B within the scaffolds, fluorescence images were stitched together to create a continuous view of the scaffold. The distribution was then quantified using the Plot Profile function in ImageJ software (version 1.48).[24]

2.7. Rhodamine B staining of silica nanoparticles

Silica nanoparticles (SiNPs) were synthesized using a modified Stöber method.[25] Briefly, 81 ml of ethanol and 24.4 mL of 28% ammonia were mixed and stirred for 30 min at 40 °C, followed by the addition of 4.2 mL tetraethoxysilane and 1 h of stirring at room temperature. The suspension was centrifuged at 4,000 × g for 5 min and washed three times with dH_2O, including 15 min of sonication per wash. The final pellets were resuspended in 2 mL of water and dried overnight at 60 °C. The morphology of SiNPs was analyzed using a Zeiss Neon40 (Germany) scanning electron microscope at an accelerating voltage of 2–5 kV. Prior to imaging, samples were carbon-coated to enhance conductivity. SiNPs were fluorescently labeled by incubation in a 20 μM Rhodamine B solution for 30 min, followed by three washes with dH_2O. To evaluate the distribution of fluorescently labeled SiNPs within the core of printed hydrogel filaments, fluorescence images were analyzed using ImageJ software. Measurements were performed at 20 distinct locations, ensuring a comprehensive representation of SiNP distribution.

2.8. Biological testing

2.8.1. Cell culture

Mesenchymal stem cells were cultured at 37 °C and 5% CO_2 in culture medium consisting of α-MEM, 10% (v/v) FBS, 1% (v/v) GlutaMAX, and 1% (v/v) P/S (10,000 U/ml and 10 mg/ml, respectively). HUVECs were cultured in culture medium consisting of Vascular Cell Basal Medium, Endothelial Cell Growth Kit-VEGF, 2% (v/v) FBS, 1% (v/v) GlutaMAX, and 1% (v/v) P/S (10,000 U/ml and 10 mg/ml, respectively). The medium was changed every 2–3 days, and subconfluent cells were detached from the culture flask using trypsin-EDTA. Only cells from passages 3–5 were used for the experiments.

2.8.2. Core bioink preparation

To evaluate cell distribution, MSCs and HUVECs were fluorescently labeled by incubating for 30 min in serum-free cell culture medium containing 1 μM CellTracker™ Deep Red or 10 μM CellTracker™ Green CMFDA. MSCs were detached and resuspended in 10% (w/v) sucrose

solution before mixing with RADA16-I solution at a concentration of 1×10^6 cells/ml. For testing viability and morphology of 3D-printed cell-laden hydrogel scaffolds, MSCs and HUVECs were detached and resuspended in 10% (w/v) sucrose solution, before mixing separately with RADA16-I solution at a concentration of 4×10^6 cells/ml.

2.8.3. Cell distribution and morphology

Printed scaffolds were crosslinked in a solution containing 150 mM $CaCl_2$ and 50 mM HEPES for 5 min, followed by three washes in culture medium. The distribution of red- and green-fluorescently labeled MSCs was evaluated after crosslinking and subsequent washing steps. The viability of bioprinted MSCs and HUVECs was evaluated after 4 days of incubation. Live cells were stained using calcein AM cell-permeant dye, and dead cells were counterstained using membrane-impermeant PI dye. Hydrogel samples were incubated in a working solution containing 2 µM calcein AM and 750 nM PI at 37°C and 5% CO_2. Then, samples were washed twice in DPBS and imaged with a Leica TCS SP8 CLSM using excitation/emission wavelengths of 494/510–540 and 535/600–640 nm, respectively. Cell morphology was evaluated on day 4 by staining actin filaments of encapsulated cells. Samples were washed twice in DPBS, then fixed in 4% paraformaldehyde for 10 min, followed by three additional washes with DPBS. Then, cells were permeabilized by submerging samples in 0.1% Triton X-100 in DPBS with gentle shaking for 30 min, followed by three additional washes in DPBS. Next, samples were incubated in a solution of phalloidin-Atto 488 (0.1 µg/ml in PBS) for 30 min, and 10 min in a solution of DAPI (20 µg/ml in PBS). After an additional three washes with DPBS, cells were imaged using a CLSM, with excitation/emission wavelengths set to 405/440–480 nm and 488/495–545 nm for DAPI and phalloidin-Atto 488, respectively.

3. Results and discussion

The present study utilized a custom-modified 3D bioprinter capable of operating three independent syringe pump extruders. The main syringe-extruder printhead, carrying a coaxial nozzle, directly fed a load-bearing MC–alginate composite hydrogel shell material (Figure 1). Two additional extruders fed a low-viscosity RADA16-I peptide-based core solution to the coaxial nozzle via tubing. The coaxial nozzle featured a screw-like design that facilitated passive mixing of the two core solutions. Spatiotemporal control over the extrusion ratio between the two core solutions and *in situ* mixing enabled the fabrication of scaffolds with a continuous cell distribution gradient. Immediately after coextrusion, the phosphate-buffered, viscous hydrogel shell enabled the self-assembly of the RADA16-I cell-laden hydrogel core, thereby producing stable cell-laden hydrogel scaffolds.

3.1. Coaxial nozzle fabrication

In the design of the coaxial nozzle print head, several requirements were considered to ensure optimal performance. A conical coaxial shell was selected to enable smooth extrusion of the highly viscous shell material, whereas narrow cylindrical geometries were selected to confine the two low-viscosity core solutions. A screw-like design was integrated within the nozzle, which has previously demonstrated excellent mixing performance

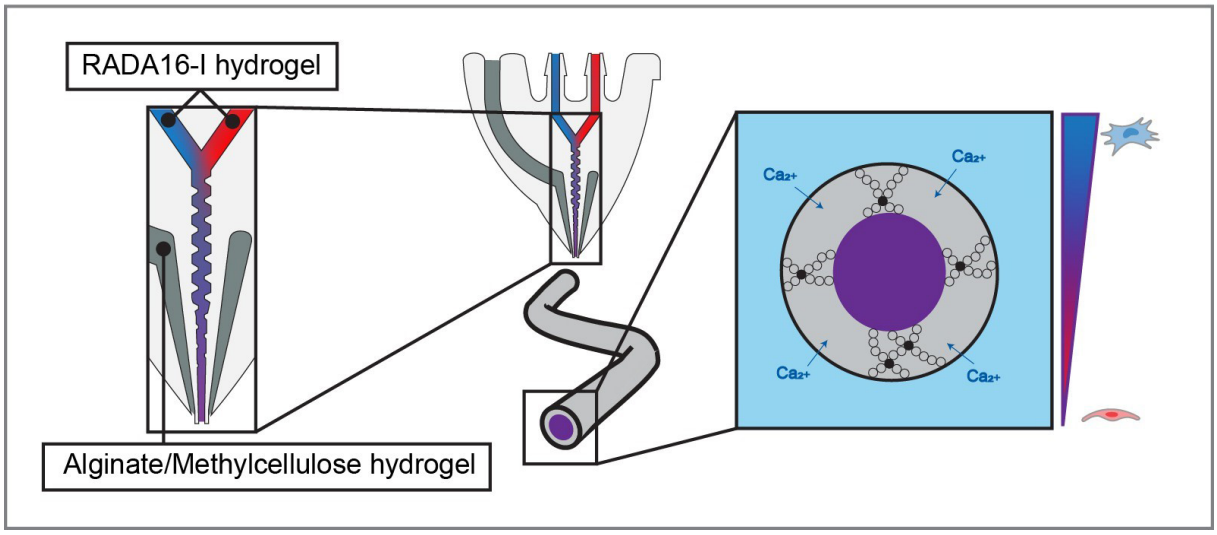

Figure 1. Schematic of core–shell 3D microfluidic bioprinting process

and high cell viability in highly viscous bioinks.[26] The diameter ratio between the core and shell at the nozzle tip was chosen to match the flow rates of the core and shell materials with the desired core–shell extrusion ratios. Additionally, the core tip was set to protrude half the shell tip's outer diameter from the coaxial nozzle. Collectively, these design criteria were critical for extruding stable filaments and avoiding mixing between the core and shell materials. An indentation in the print head allowed the coaxial nozzle to fit securely (Figure 2A[i]). A blunt tip on a syringe, inserted directly into the print head, fed the viscous shell material into the coaxial nozzle. Two horizontally positioned syringe pump extruders supplied the low-viscosity core solutions. The core tip protruded by approximately 500 μm from the coaxial nozzle (Figure 2A[ii, iii]). The coaxial nozzle tip had an outer diameter of 1 mm, an inner diameter of 320 μm, and a wall thickness of 180 μm separating the core and shell channels (Figure 2A[iv]). Additionally, a cross-sectional cut of the nozzle was printed to demonstrate the quality of the internal features of the screw-like mixer (Figure 2B[i]). Microscopic images showed good preservation of intricate features, with channel widths matching the design and good integrity of the mixing unit (Figure 2B[ii, iii]).

3.2. Computational analysis of mixing performance

To evaluate the effectiveness of the passive mixing unit, computational analysis was performed to calculate the concentration field of a dilute solute within a liquid solvent. The transport of the solute was compared between two channel geometries: one featuring a screw-like mixer and another with a straight channel (Figure 2C[i, ii]). Surface plots of solute concentration across these channels revealed uniform mixing in the screw-like mixing unit. In contrast, the straight channel configuration showed reduced passive mixing, relying primarily on diffusion rather than convection for solute transport. Line plots of dilute-solute concentration showed that the solute was evenly distributed after passing through the mixing unit for all tested extrusion ratios (Figure 2C[iii]). In contrast, straight channels resulted in inadequate mixing, with the poorest mixing observed at the 1:1 extrusion ratio.

It is important to note that the internal nozzle geometry affects the transition time and transition distance between extruded materials. The mixing unit in this study is integrated within the coaxial nozzle, where geometric parameters are constrained by the need to co-extrude a low-viscosity core and a highly viscous shell material. The effective mixing length is therefore limited by the inner needle position and channel dimensions, which were optimized to reduce transition distance while preserving filament stability. Further reduction of the channel diameter could shorten the transition length but may lead to increased core flow velocity, potentially compromising shape fidelity and causing core material leakage.[21]

3.3. Empirical gradient and mixing characterization in 3D-printed scaffolds

The ability to fabricate hydrogel scaffolds with a continuous material gradient between two materials was empirically tested (Figure 3A). The scaffold design comprised two layers: the base layer was printed exclusively from shell material, providing a stable foundation, while the second layer was printed with the shell and core extrusion set to 70% and 30%, respectively. Throughout the second layer, the relative extrusion of the core materials was gradually shifted in 10% increments to establish a smooth transition between the two materials. Images of scaffolds taken immediately after printing demonstrated a gradual transition between the two core materials (Figure 3A[i]). Similarly, the red fluorescence signal of Rhodamine B encapsulated in the core material displayed a gradient across ionically crosslinked scaffolds (Figure 3A[ii, iii]). Plot profiles from image data showed the Rhodamine B fluorescence signal across the scaffold structure (Figure 3A[iv]). The fluorescence intensity peaked only shortly after the extrusion of the Rhodamine B-stained material, due to the time required to establish full flow of the core material. Subsequently, the fluorescence intensity gradually declined as an incremental transition to the colorless core material occurred. The results confirmed the successful fabrication of scaffolds with a continuous material gradient, demonstrating the feasibility of precisely controlling the transition between different core materials.

Furthermore, the performance of the screw-like mixing unit was evaluated using SiNPs (Figure 3B). The small size and hydrophilic nature of the SiNPs allowed for their extrusion when encapsulated in a hydrogel and enabled staining with Rhodamine B (Figure 3B[i]). Hydrogel scaffolds were printed using a core extrusion ratio of 1:1, with one cartridge containing RADA16-I with SiNPs and the other containing RADA16-I alone (Figure 3B[ii]). Microscopic images showed that SiNPs were retained in the core structure and evenly distributed throughout the hydrogel scaffold (Figure 3B[iii, iv, v]). Plot profiles showing the average SiNP distribution across printed filaments indicated a relatively even distribution, with a tendency for SiNPs to accumulate along the sides (Figure 3B[vi]). These findings validate the screw-like mixing unit's ability to evenly distribute particulate matter within the filament core of printed hydrogel scaffolds.

While the present computational and experimental results confirm efficient mixing and continuous gradient

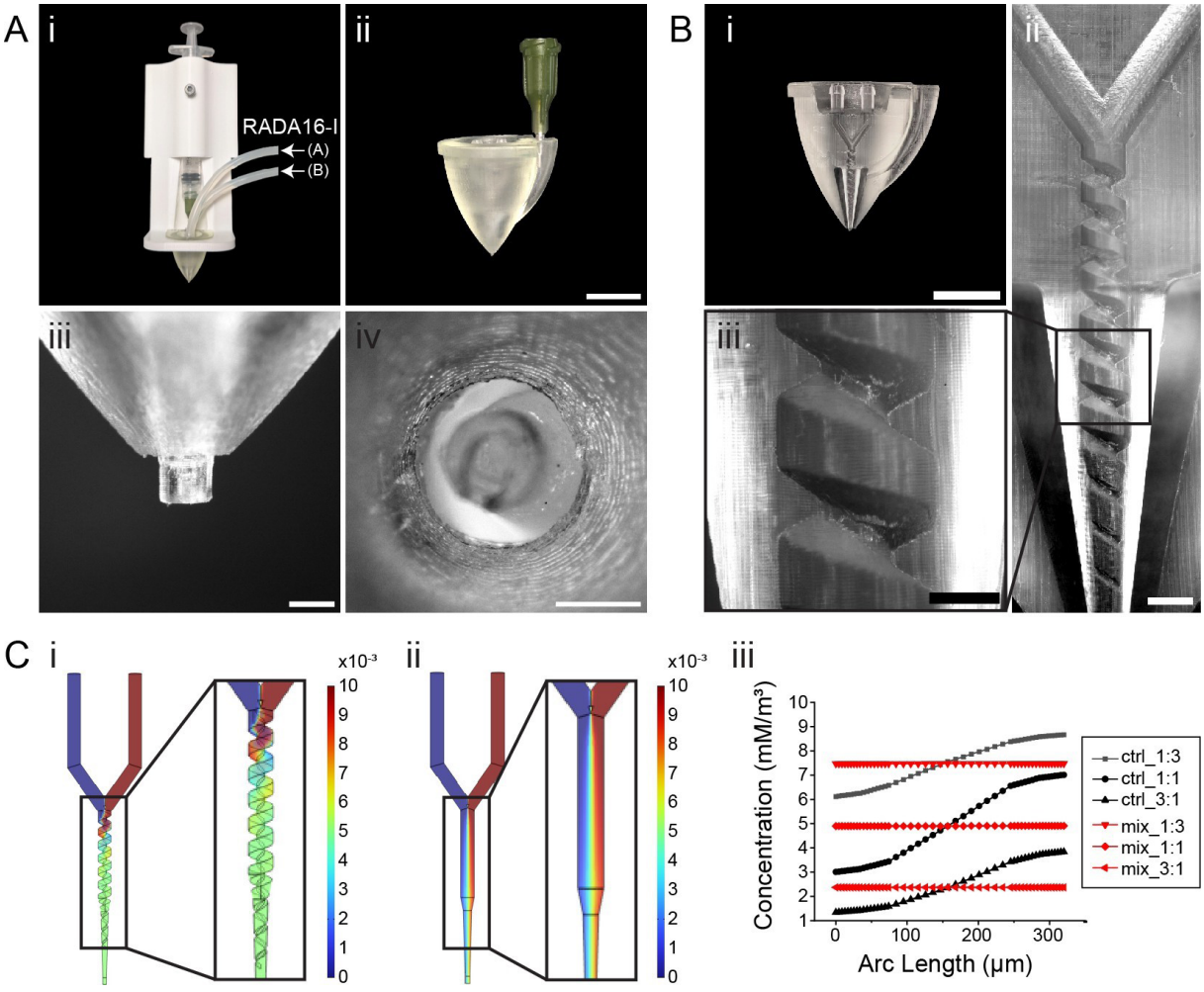

Figure 2. Fabrication of coaxial microfluidic nozzles and computational fluid dynamics analysis. (A) (i) Print head with coaxial nozzle fitted into a dedicated slot, with a syringe inserted to feed the shell material and tubing connected to supply the core material. (ii) 3D printed coaxial nozzle with blunt tip inserted. Scale bar: 5 mm; magnification: 40×. (iii) Side view of the coaxial nozzle tip. Scale bar: 500 μm; magnification: 200×. (A, iv) Frontal view of the coaxial nozzle tip. Scale bar: 500 μm; magnification: 200×. (B) (i) Cross-section of 3D printed coaxial nozzle. Scale bar: 5 mm; magnification: 40×. (ii) Mixing unit of the coaxial nozzle. Scale bar: 1 mm; magnification: 100×. (iii) Close-up of mixing unit. Scale bar: 500 μm; magnification: 200×. (C) Computational simulation of fluid mixing (i) with a mixing unit and (ii) in a straight channel. (iii) Line plot comparing fluid mixing between the two nozzle configurations at different extrusion ratios.

formation, a quantitative assessment of the transition length (i.e., the spatial distance over which the composition changes) was not performed. In microfluidic gradient systems, such parameters are commonly evaluated using image-based approaches.[27] In the present coaxial extrusion setup, such analysis is limited by the enclosed nozzle geometry and the coupled flow of core and shell materials. Nevertheless, the spatial evolution of fluorescence intensity and particle distribution qualitatively confirms a continuous and controllable gradient.

3.4. Bioprinting

3.4.1. Distribution gradient of encapsulated mesenchymal stem cells

To fabricate scaffolds with continuous cell-laden gradients, MSCs were labeled with either red- or green-fluorescent CellTracker™ dye, suspended in RADA16-I solutions (1×10^6 cells/ml), and loaded into separate cartridges feeding the core material. The cell distribution in 3D bioprinted hydrogel scaffolds was evaluated using confocal

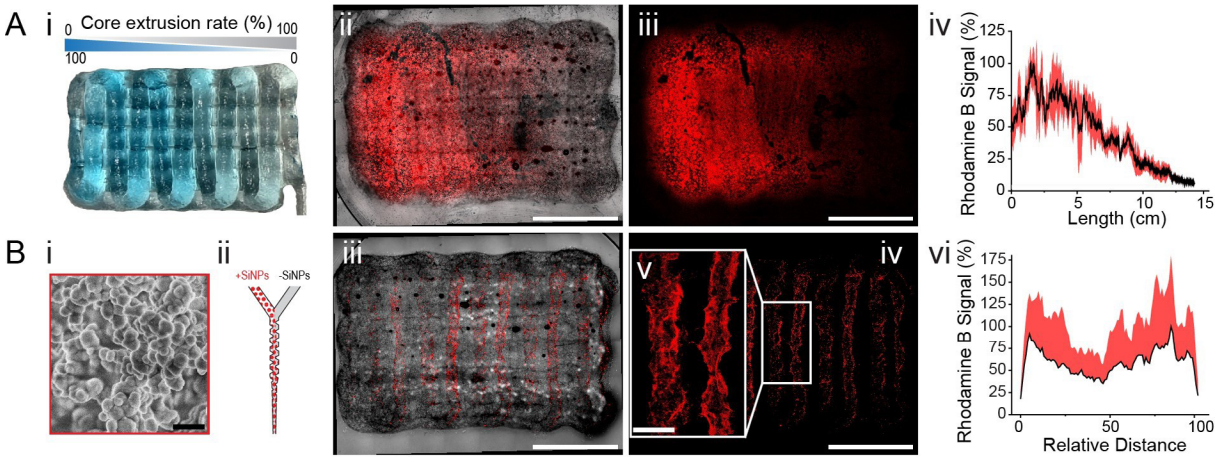

Figure 3. Evaluation of gradient distribution and mixing performance of 3D printed hydrogel scaffolds. (A) (i) Hydrogel scaffolds were printed with a gradient between two core solutions, dyed blue and colorless, to illustrate the gradient distribution. (ii) Merged bright-field and fluorescence images of a 3D printed hydrogel scaffold, with one core dyed with Rhodamine B to illustrate mixing performance. (iii) Fluorescence image of the same scaffold. Scale bar: 5 mm; magnification: 40×. (iv) Plot profile showing the distribution of Rhodamine B across the length of the hydrogel scaffold (n = 3). (B) (i) Electron microscope image of silica nanoparticles (SiNPs). Scale bar: 500 nm; magnification: 200×. (ii) Schematic of the experimental setup for testing the mixing performance of a coaxial nozzle. The RADA16-I core solution, with and without SiNPs, was extruded at an equal ratio. (iii) Merged bright-field and fluorescence images of a 3D-printed hydrogel scaffold, showing the distribution of Rhodamine B-dyed SiNPs within the core of the extruded filaments. (iv) Fluorescence image of the same scaffold. Scale bar: 5 mm; magnification: 40×. (v) Extruded filament core at higher magnification. Scale bar: 1 mm; magnification: 100×. (vi) Plot profile showing the distribution of Rhodamine B-labeled SiNPs across the width of extruded filaments (n = 3).

fluorescence microscopy (Figure 4A–C). Within the central region of the hydrogel scaffold, encapsulated MSCs gradually transitioned between green- and red-fluorescent populations. To capture the transition in cell composition along the printing path, higher-magnification images were taken of regions corresponding to extrusion ratios of 100:0, 50:50, and 0:100 (Figure 4C). The images were taken with careful consideration of the printing length required to achieve the desired composition switch.

3.4.2. Fabrication of continuous HUVEC–MSC co-culture gradient

By replicating the previously established scaffold design and printing procedure, a spatial HUVEC–MSC co-culture gradient was generated (Figure 4D and 4E). Co-culture of MSCs and endothelial cells has been extensively studied for prevascularization in tissue engineering; MSCs provide paracrine and structural support that promotes the formation of prevascular networks.[28] This interaction is largely mediated by paracrine signaling, with MSCs secreting pro-angiogenic factors that enhance endothelial proliferation, migration, and network formation, while endothelial cells in turn regulate MSC behavior through growth factor signaling and direct cell–cell communication. Such bidirectional crosstalk has been widely exploited in tissue engineering to promote prevascularization and improve integration of engineered constructs.[29]

Red-labeled HUVECs and unlabeled MSCs were suspended in RADA16-I solution (4 × 10^6 cells/ml) and loaded into separate cartridges. Following printing and four days of cultivation, live/dead staining indicated that most cells remained viable (Figure 4D). This observation is consistent with our previous work demonstrating shear stress during nozzle extrusion of low-viscosity RADA16-I precursor solution to be well below the threshold reported to significantly impair cell viability.[23,30,31] However, differences in cell distribution and organization were observed between regions containing HUVECs, MSCs, or a mixture of both. In regions containing MSCs, actin-stained cells formed aggregates that occasionally interconnected (Figure 4E). A similar tendency for spontaneous cell aggregation in RADA16-I hydrogels when supplemented with MC and sucrose has been observed previously.[23] Immediate cell aggregation after cell encapsulation suggests that early physicochemical interactions drive initial changes in organization rather than cell-driven remodeling. In this context, MC and sucrose can promote polymer-induced aggregation through depletion interactions and reduced electrostatic repulsion, as reported for macromolecular crowding environments.[32]

In regions where both cell populations were present at approximately equal ratios, smaller MSC aggregates were surrounded by more homogeneously distributed HUVEC networks. In contrast, regions containing only

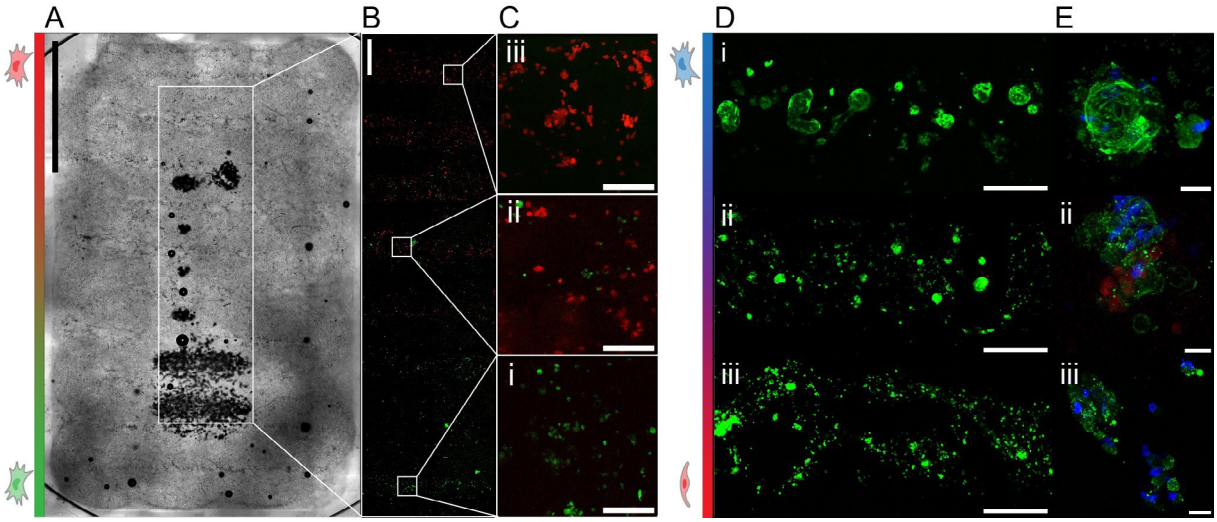

Figure 4. Viability and distribution of encapsulated mesenchymal stem cells (MSCs) and human umbilical vein endothelial cell (HUVEC)–MSC co-cultures. (A) Bright-field image of the entire hydrogel scaffold. Scale bar: 5 mm; magnification: 40×. (B) Fluorescence image showing the distribution of red- and green-labeled MSCs throughout the printed scaffold. Scale bar: 1 mm; magnification: 100×. (C) Higher-magnification fluorescence image showing regions containing (i) primarily green-labeled cells, (ii) mixed green- and red-labeled cells, and (iii) primarily red-labeled cells. Scale bar: 200 μm; magnification: 600×. (D) Live (green)/dead (red) staining of MSCs and HUVECs after four days of incubation, showing regions containing (i) predominantly MSCs, (ii) a mixed population of MSCs and HUVECs, and (iii) predominantly HUVECs. Scale bar: 500 μm; magnification: 40×. (E) Fluorescence images showing cell morphology (blue: DAPI staining, nuclei; green: Phalloidin-ATTO, actin cytoskeleton) in regions containing (i) predominantly MSCs, (ii) a mixed population of MSCs and HUVECs, and (iii) predominantly HUVECs. Scale bar: 200 μm; magnification: 600×.

HUVECs exhibited a more spread-out morphology, forming continuous cellular networks. These observations indicate that while MC modulates early cell organization, it does not impair endothelial network formation and may facilitate localized cell–cell interactions that contribute to the spatial structuring of the co-culture. However, it should be noted that these findings are based on early time points (day 4). Although actin staining suggests the formation of prevascular networks, further analysis of endothelial markers would be required to confirm the development of functional prevascular structures.

4. Conclusion

In this study, we configured a microfluidic coaxial 3D bioprinter setup to create hydrogel scaffolds with continuous gradients of cell populations and materials. Integrating a screw-like mixer within the coaxial nozzle enabled seamless mixing of low-viscosity, low-mechanical-strength RADA16-I bioinks. The load-bearing MC–alginate hydrogel shell enabled 3D printing of the soft self-assembling peptide bioink while supporting shape fidelity and nutrient diffusion during cultivation. The scaffolds demonstrated cell-type-specific organization, highlighting the ability of cells to freely move, adapt their morphology, and function effectively within the bioink. This method has the potential to mimic the dynamic and biomimetic environment of native tissues. Future studies should focus on integrating additional cell types, further refining gradient complexity, and evaluating the functional performance of the resulting tissue-engineered constructs.

Acknowledgments

None.

Funding

The authors would like to thank MICIU/AEI 10.13039/501100011033 and FEDER, UE for funding project PID2022-137962OB-I00, MICIU/AEI/10.13039/501100011033 and Union Europea NextGenerationEU/PRTR for funding project PLEC2022-009279, and Programme/Generalitat de Catalunya (2021 SGR 00565).

Conflict of interest

The authors declare they have no competing interests.

Author contributions

Conceptualization: Miguel A. Mateos-Timoneda
Formal analysis: Maximilian Jergitsch, Miguel A. Mateos Timoneda
Funding acquisition: Roman A. Perez, Miguel A. Mateos-

Timoneda
Investigation: Maximilian Jergitsch, Soledad Perez-Amodio, Luis M. Delgado
Methodology: Maximilian Jergitsch, Soledad Perez-Amodio, Luis M. Delgado
Project administrations: Miguel A. Mateos-Timoneda
Writing–original draft: Maximilian Jergitsch
Writing–review & editing: All authors

Ethics approval and consent to participate

Not applicable.

Consent for publication

Not applicable.

Availability of data

Data is available from the corresponding author upon reasonable request.

References

1. Mota C, Camarero-Espinosa S, Baker MB, Wieringa P, Moroni L. Bioprinting: From Tissue and Organ Development to *in Vitro* Models. *Chem Rev*. 2020;120(19):10547-10607.

   doi: 10.1021/acs.chemrev.9b00789

2. Dai W, Wu T, Leng X, *et al*. Advances in biomechanical and biochemical engineering methods to stimulate meniscus tissue. *Am J Transl Res*. 2021;13(8):8540-8560.

3. Mukund K, Subramaniam S. Skeletal muscle: A review of molecular structure and function, in health and disease. *WIREs Mech Dis*. 2019;12(1).

   doi: 10.1002/wsbm.1462

4. Santos-Beato P, Midha S, Pitsillides AA, Miller A, Torii R, Kalaskar DM. Biofabrication of the osteochondral unit and its applications: Current and future directions for 3D bioprinting. *J Tissue Eng*. 2022;13.

   doi: 10.1177/20417314221133480

5. Hama R, Reinhardt JW, Ulziibayar A, Watanabe T, Kelly J, Shinoka T. Recent Tissue Engineering Approaches to Mimicking the Extracellular Matrix Structure for Skin Regeneration. *Biomimetics*. 2023;8(1):130.

   doi: 10.3390/biomimetics8010130

6. Fang L, Lin X, Xu R, *et al*. Advances in the Development of Gradient Scaffolds Made of Nano-Micromaterials for Musculoskeletal Tissue Regeneration. *Nano-Micro Lett*. 2024;17(1).

   doi: 10.1007/s40820-024-01581-4

7. Niu X, Li N, Du Z, Li X. Integrated gradient tissue-engineered osteochondral scaffolds: Challenges, current efforts and future perspectives. *Bioact Mater*. 2023;20:574-597.

   doi: 10.1016/j.bioactmat.2022.06.011

8. Murphy SV, Atala A. 3D bioprinting of tissues and organs. *Nat Biotechnol*. 2014;32(8):773-785.

   doi: 10.1038/nbt.2958

9. Zhang YS, Haghiashtiani G, Hübscher T, *et al*. 3D extrusion bioprinting. *Nat Rev Methods Primers*. 2021;1(1).

   doi: 10.1038/s43586-021-00073-8

10. Jergitsch M, Mateos-Timoneda MA. 3D extrusion bioprinting: rational bioink design and advanced fabrication techniques. *Trends Biotechnol*. 2026;44(2):378-388.

    doi: 10.1016/j.tibtech.2025.06.008

11. Cui X, Li J, Hartanto Y, *et al*. Advances in Extrusion 3D Bioprinting: A Focus on Multicomponent Hydrogel-Based Bioinks. *Adv Healthc Mater*. 2020;9(15).

    doi: 10.1002/adhm.201901648

12. Levato R, Visser J, Planell JA, Engel E, Malda J, Mateos-Timoneda MA. Biofabrication of tissue constructs by 3D bioprinting of cell-laden microcarriers. *Biofabrication*. 2014;6(3):035020.

    doi: 10.1088/1758-5082/6/3/035020

13. Kilian D, Ahlfeld T, Akkineni AR, Bernhardt A, Gelinsky M, Lode A. 3D Bioprinting of osteochondral tissue substitutes – *in vitro*-chondrogenesis in multi-layered mineralized constructs. *Sci Rep*. 2020;10(1).

    doi: 10.1038/s41598-020-65050-9

14. Bittner SM, Smith BT, Diaz-Gomez L, *et al*. Fabrication and mechanical characterization of 3D printed vertical uniform and gradient scaffolds for bone and osteochondral tissue engineering. *Acta Biomater*. 2019;90:37-48.

    doi: 10.1016/j.actbio.2019.03.041

15. Malda J, Visser J, Melchels FP, *et al*. 25th Anniversary Article: Engineering Hydrogels for Biofabrication. *Adv Mater*. 2013;25(36):5011-5028.

    doi: 10.1002/adma.201302042

16. Ouyang L. Pushing the rheological and mechanical boundaries of extrusion-based 3D bioprinting. *Trends Biotechnol*. 2022;40(7):891-902.

    doi: 10.1016/j.tibtech.2022.01.001

17. Colosi C, Shin SR, Manoharan V, *et al*. Microfluidic Bioprinting of Heterogeneous 3D Tissue Constructs Using Low-Viscosity Bioink. *Adv Mater*. 2015;28(4):677-684.

    doi: 10.1002/adma.201503310

18. Susapto HH, Alhattab D, Abdelrahman S, *et al*. Ultrashort Peptide Bioinks Support Automated Printing of Large-Scale Constructs Assuring Long-Term Survival of Printed Tissue Constructs. *Nano Lett*. 2021;21(7):2719-2729.

doi: 10.1021/acs.nanolett.0c04426

19. Idaszek J, Costantini M, Karlsen TA, *et al*. 3D bioprinting of hydrogel constructs with cell and material gradients for the regeneration of full-thickness chondral defect using a microfluidic printing head. *Biofabrication*. 2019;11(4):044101.

doi: 10.1088/1758-5090/ab2622

20. Ravanbakhsh H, Karamzadeh V, Bao G, Mongeau L, Juncker D, Zhang YS. Emerging Technologies in Multi-Material Bioprinting. *Adv Mater*. 2021;33(49).

doi: 10.1002/adma.202104730

21. Jergitsch M, Soiunov R, Selinger F, *et al*. Fabrication and validation of an affordable DIY coaxial 3D extrusion bioprinter. *Sci Rep*. 2025;15(1).

doi: 10.1038/s41598-025-06478-9

22. Liu W, Zhong Z, Hu N, *et al*. Coaxial extrusion bioprinting of 3D microfibrous constructs with cell-favorable gelatin methacryloyl microenvironments. *Biofabrication*. 2018;10(2):024102.

doi: 10.1088/1758-5090/aa9d44

23. Jergitsch M, Perez-Amodio S, Delgado LM, Perez RA, Mateos-Timoneda MA. 3D coaxial bioprinting of RADA16-I self-assembling peptide hydrogel. *Mater Today Bio*. 2026;37:102900.

doi: 10.1016/j.mtbio.2026.102900

24. Schneider CA, Rasband WS, Eliceiri KW. NIH Image to ImageJ: 25 years of image analysis. *Nat Methods*. 2012;9(7):671-675.

doi: 10.1038/nmeth.2089

25. Stöber W, Fink A, Bohn E. Controlled growth of monodisperse silica spheres in the micron size range. *J Colloid Interface Sci*. 1968;26(1):62-69.

doi: 10.1016/0021-9797(68)90272-5

26. Dani F, Ahlfeld T, Albrecht F, *et al*. Homogeneous and Reproducible Mixing of Highly Viscous Biomaterial Inks and Cell Suspensions to Create Bioinks. *Gels*. 2021;7(4):227.

doi: 10.3390/gels7040227

27. Wang M, Li W, Mille LS, *et al*. Digital Light Processing Based Bioprinting with Composable Gradients. *Adv Mater*. 2021;34(1).

doi: 10.1002/adma.202107038

28. Shafiee S, Shariatzadeh S, Zafari A, Majd A, Niknejad H. Recent Advances on Cell-Based Co-Culture Strategies for Prevascularization in Tissue Engineering. *Front Bioeng Biotechnol*. 2021;9.

doi: 10.3389/fbioe.2021.745314

29. Mazloomnejad R, Babajani A, Kasravi M, *et al*. Angiogenesis and Re-endothelialization in decellularized scaffolds: Recent advances and current challenges in tissue engineering. *Front Bioeng Biotechnol*. 2023;11.

doi: 10.3389/fbioe.2023.1103727

30. Ouyang L, Yao R, Zhao Y, Sun W. Effect of bioink properties on printability and cell viability for 3D bioplotting of embryonic stem cells. *Biofabrication*. 2016;8(3):035020.

doi: 10.1088/1758-5090/8/3/035020

31. Ahlfeld T, Guduric V, Duin S, *et al*. Methylcellulose – a versatile printing material that enables biofabrication of tissue equivalents with high shape fidelity. *Biomater Sci*. 2020;8(8):2102-2110.

doi: 10.1039/d0bm00027b

32. Gonzalez La Corte S, Stevens CA, Cárcamo-Oyarce G, Ribbeck K, Wingreen NS, Datta SS. Morphogenesis of bacterial cables in polymeric environments. *Sci Adv*. 2025;11(3).

doi: 10.1126/sciadv.adq7797